Advanced Composite Materials
Publication details, including instructions for authors and subscription information:
http://www.tandfonline.com/loi/tacm20

Characterization of tensile damage progress in stitched CFRP laminates

Akinori Yoshimura [a], Shigeki Yashiro [b], Tomonaga Okabe [c] & Nobuo Takeda [d]

[a] Graduate school of Frontier Sciences, The University of Tokyo, 5-1-5 Kashiwanoha, Kashiwa, Chiba 277-8561, Japan

[b] Research Institute of Instrumentation Frontier, National Institute of Advanced Industrial Science and Technology (AIST), 1-1-1 Umezono, Tsukuba, Ibaraki 305-8568, Japan

[c] Department of Aerospace Engineering, Tohoku University, 6-6-01 Aobayama, Aoba-ku, Sendai 980-8579, Japan

[d] Graduate school of Frontier Sciences, The University of Tokyo, 5-1-5 Kashiwanoha, Kashiwa, Chiba 277-8561, Japan

Version of record first published: 02 Apr 2012.

Adv. Composite Mater., Vol. 16, No. 3, pp. 223–244 (2007)

Also available online - www.brill.nl/acm

Characterization of tensile damage progress in stitched CFRP laminates

AKINORI YOSHIMURA [1,*], SHIGEKI YASHIRO [2], TOMONAGA OKABE [3] and NOBUO TAKEDA [1]

[1] *Graduate school of Frontier Sciences, The University of Tokyo, 5-1-5 Kashiwanoha, Kashiwa, Chiba 277-8561, Japan*
[2] *Research Institute of Instrumentation Frontier, National Institute of Advanced Industrial Science and Technology (AIST), 1-1-1 Umezono, Tsukuba, Ibaraki 305-8568, Japan*
[3] *Department of Aerospace Engineering, Tohoku University, 6-6-01 Aobayama, Aoba-ku, Sendai 980-8579, Japan*

Received 13 July 2006; accepted 10 November 2006

Abstract—This study experimentally and numerically investigated the tensile damage progress in stitched laminates. In particular, it focused on the effects of stitching on the damage progress. First, we experimentally confirmed that ply cracks and delamination appeared under load regardless of stitching. We then performed damage-extension simulation for stitched laminates using a layer-wise finite element model with stitch threads as beam elements, in which the damage (ply cracks and delamination) was represented by cohesive elements. A detailed comparison between observation and the simulated results confirmed that stitching had little effect on the onset and accumulation of ply cracks. Furthermore, we demonstrated that the stitch threads significantly suppressed the extension of the delamination.

Keywords: Stitched laminate composite; damage; tensile test; finite element analysis; damage extension simulation; transverse crack; delamination.

1. INTRODUCTION

Fiber reinforced plastic (FRP) laminates have been used as the structural components in aerospace structures because FRP laminates have good mechanical properties such as high specific stiffness and strength. However, because of the low interlaminar fracture toughness of the FRP, out-of-plane impacts easily generate delamination, and the delamination greatly reduces the compressive strength. A stitched

Edited by the JSCM.

*To whom correspondence should be addressed. E-mail: yoshimura@smart.k.u-tokyo.ac.jp

laminate, in which the stitch threads (carbon tows, aramid tows, etc.) are directed along the through-thickness direction, is thought to be a promising solution for this problem.

Numerous studies have been conducted on the interlaminar fracture toughness tests (DCB, ENF, etc.) of stitched laminates, and the numerical simulations of the tests [1–5]. The results revealed that the stitch threads bridged the delaminated sublaminates, and thus the interlaminar fracture toughness was significantly increased. In addition, the stitching increased the post-impact compressive strength of the laminates [6]. However, the studies on the in-plane properties of the stitched laminates revealed that stitching shortened the fatigue life [7, 8] and slightly decreased the tensile stiffness and strength [6, 7, 9].

Moreover, Warrior *et al.* [10] found that the stiffness of the stitched laminates gradually decreased when tensile load increased. They suggested that this was due to the damage that occurred in the laminates. However, most of the previously performed studies on the stitched laminates focused only on the macroscopic mechanical properties. Thus, the onset and progress of damage have not been discussed sufficiently. In conventional (unstitched) laminates, internal damage such as ply crack and delamination occurs under tensile loading, and the cracks and delaminations affect each other and extend until final failure [11, 12]. The damage evolution has effects on the macroscopic stiffness and strength. Thus, for stitched laminates, an understanding of the damage progress is necessary to confirm the design and the reliability of the structure.

The present study investigates the tensile damage progress in stitched CFRP laminates both experimentally and numerically. This paper is organized as follows. In Section 2, a tension test is described and the experimentally observed damage progress is reported. In Section 3, we describe the numerical method that can stably simulate the crack extension in the linear elastic body [13]. This method is based on finite element analysis with cohesive elements. In Section 4, the simulated crack extension is compared with the theoretical solution to validate the numerical method. Finally, we perform the numerical simulation and discuss the effect of the stitching on the damage progress in Section 5.

2. EXPERIMENT

2.1. Experimental procedure

In this research, carbon-fiber stitched CFRP laminates (Toyota Industries Corp.) [14] were used. Carbon-fiber tows (T800-12kf, Toray Industries Inc.) were used as the inplane tows. The stacking configuration was $[-45/45/0_3/90_4]_s$. Carbon-fiber tows (TR-40-2kf, Mitsubishi Rayon Co. Ltd.) were used as the stitch threads. Figure 1 illustrates the stitching pattern. Stitch threads ran along the 0° direction of the in-plane tows. For the matrix, bismaleimide resin (Cycom5250-4RTM, Cytec Engineered Inc.) was employed. The material was impregnated and molded by the

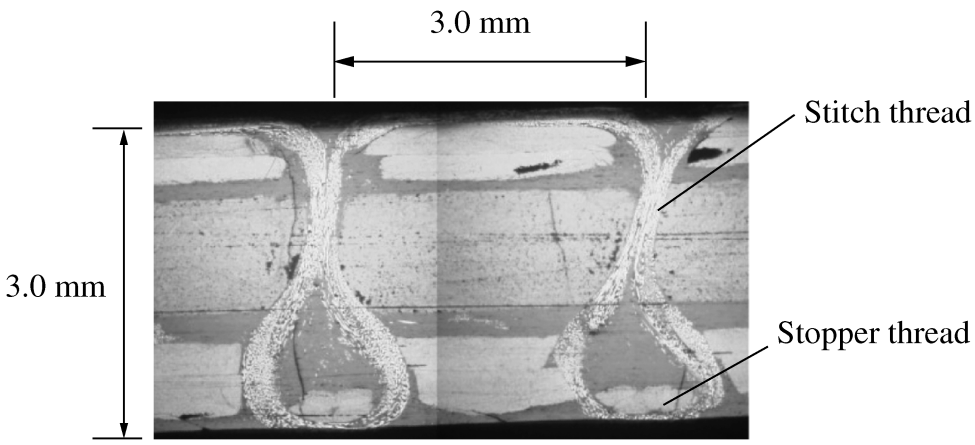

Figure 1. Cross-section of the laminate along a stitch thread.

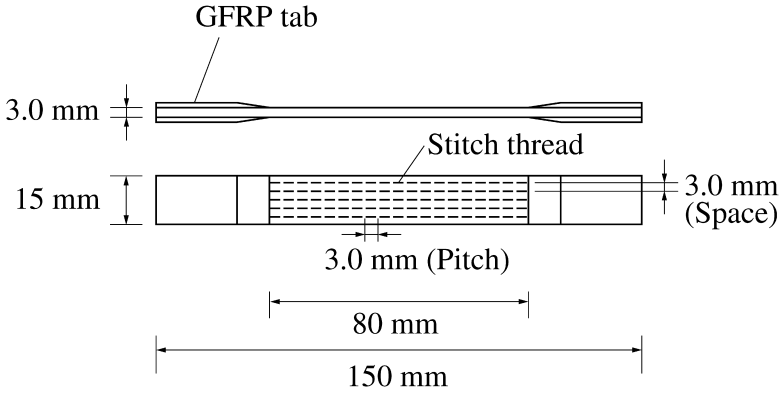

Figure 2. Dimensions of the specimen. Stitch pitch and stitch space were both 3.0 mm.

Resin Transfer Molding (RTM) method. For comparison, unstitched laminates were also prepared. The fabrication procedure of the unstitched laminates was the same as that of the stitched laminates without the stitching process. All material was cut to rectangular specimens. The dimensions of the specimens are illustrated in Fig. 2. The stitch space was 3.0 mm, and the stitch pitch was 3.0 mm. Tapered GFRP tabs were glued to the both ends of the specimens. The distance from one tab to the other (gauge length) was 80 mm.

First, the monotonic tensile tests were conducted for seven stitched and five unstitched specimens at room temperature. In the tests, the load was applied monotonically until specimen failure, and then tensile stiffness and strength were measured. The tensile load–unload tests were also conducted for three stitched and three unstitched specimens to observe the damage progress. For both tests, a tensile test machine (Instron 5582, Instron Corp.) was employed. The crosshead speed was 0.1 mm/min and the applied load was measured by built-in load cell. In the stitched laminate, the surface of the specimen was not strained uniformly because the stitch

threads disturbed the strain field. Therefore, we attached four strain gauges and an extensometer (gauge length 50 mm) to the specimen. We regarded the average of these five values as an applied strain, ε.

In the load–unload tests, the specimen was unloaded in strain increments of 0.05%, and the damage was observed from the polished edge of the specimen using a digital microscope. In addition, the specimens were ultrasonically C-scanned by using the scanning acoustic microscope (UH-3, Olympus Corporation) in 0.2% strain increments to observe the delamination progress.

2.2. Experimental results

Figure 3(a) depicts the results of the monotonic tensile tests. The average tensile stiffness and average strength of the stitched specimens were lower than those of unstitched ones, but the dispersion was larger. Because of the stacking configuration used in this study, the 0° fibers bore most of the load applied to the specimen. The volume fraction of the 0° fibers (V_{f0}) of the stitched (unstitched) specimen was 0.142 $\pm$ 0.020 (0.165 $\pm$ 0.001). This difference was not negligible. Therefore, we defined the bundle stress $\hat{\sigma}$ to remove the effect of V_{f0}. Bundle stress is the hypothetical stress calculated under the assumption that the load is borne by the 0° fibers only. The bundle stress is calculated as

$$\hat{\sigma} = \frac{\sigma}{V_{f0}}, \tag{1}$$

where σ is the stress applied to the specimen. Figure 3(b) indicates the bundle stiffness and bundle strength. When the effect of the V_{f0} was removed, it became clear that the stitching did not have any effect on the initial stiffness, but reduced the strength. Note that the reduction of the tensile strength was greater than that of the stiffness in the results from the literature, and our results followed the same trend.

Figure 4 presents the damage observed from the polished edge. In both stitched and unstitched specimens, multiple cracks occurred in the 90° ply at about 0.4% strain, and delamination occurred at the 0°/90° interface at 0.6% strain. Crack opening displacements (COD) of delaminations grew quite large in the unstitched specimens. However, the COD of the delaminations were relatively small in the stitched specimens.

Figure 5 plots the crack densities in the 90° plies as functions of the applied strain. The crack density was defined as the number of observed cracks divided by the gauge length. Crack density began to increase sharply at 0.5% strain, and after reaching 0.7% strain, the density continued to increase modestly. Note that the values of the crack densities were not equal to zero at the beginning of the tests because thermal cracks occurred during molding.

Delaminations observed using an ultrasonic C-scan are presented in Fig. 6. In both stitched and unstitched specimens, delamination occurred at 0.6 % strain at the free edges of the specimen. The delaminations extended in the width direction toward the center of the specimens. In the unstitched specimens, delaminations extended

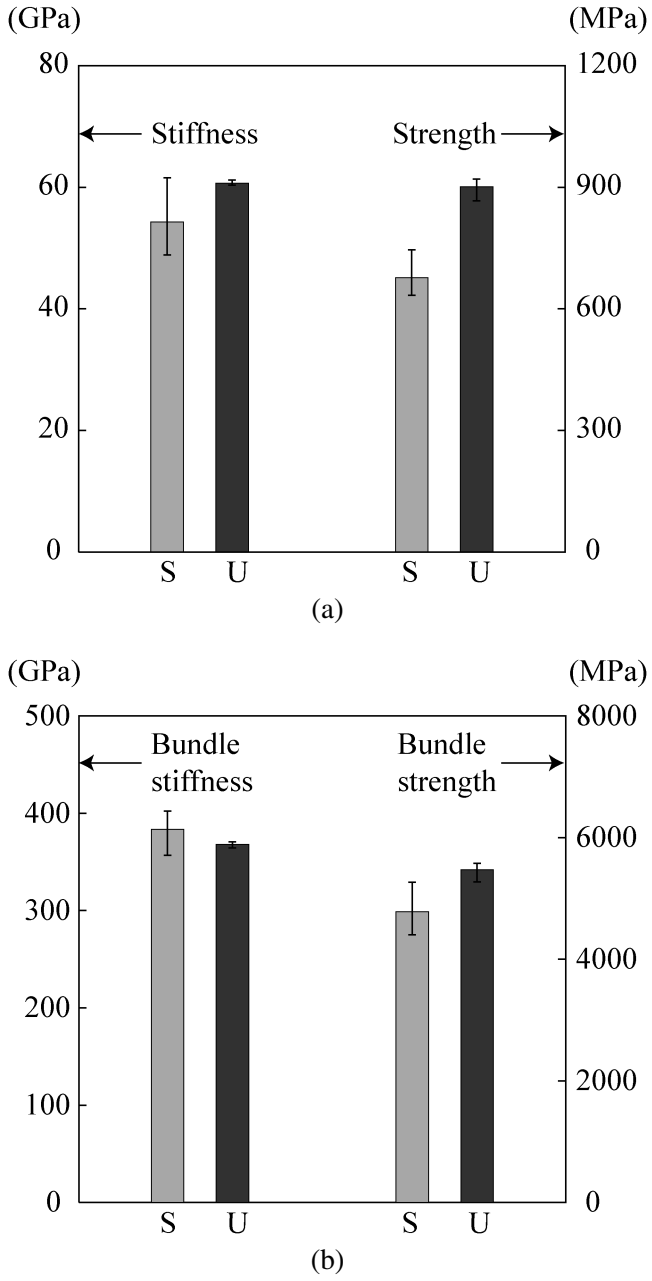

Figure 3. Comparison of results in the static tensile tests between the stitched specimens (S) and the unstitched specimens (U). (a) Stiffness and strength. (b) Bundle stiffness and bundle strength.

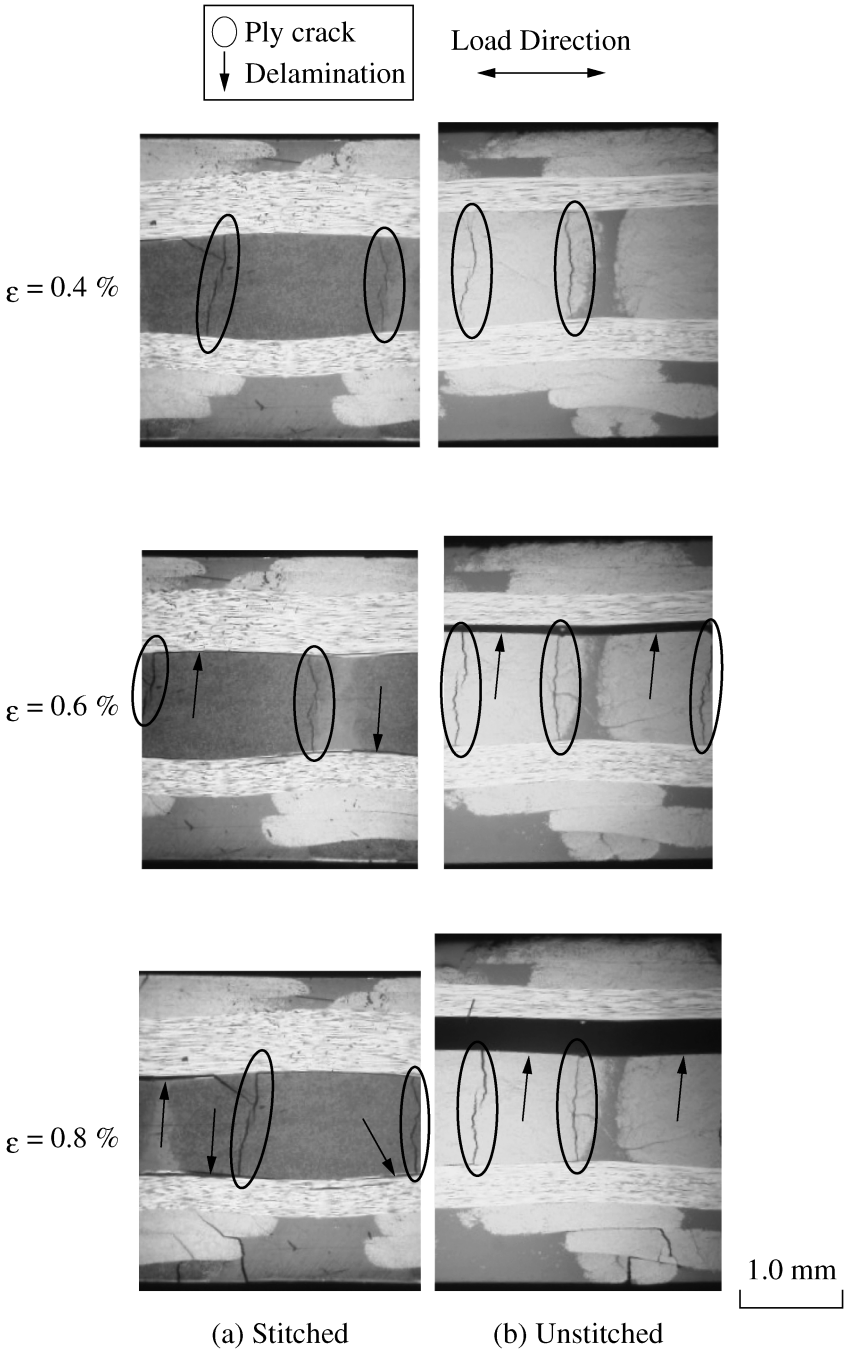

Figure 4. Observed damage states. Ply cracks were observed in the 90° ply at 0.4% strain, and delamination appeared at 0.6% strain at the 0°/90° ply interface.

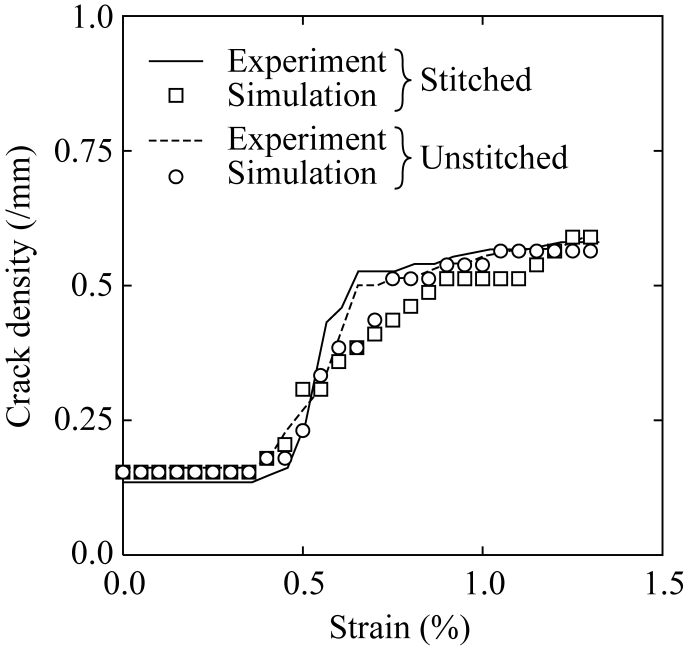

Figure 5. Measured and simulated results of ply crack density as a function of the applied strain.

rapidly with increasing strain. However, in the stitched specimens, the progress of the delaminations stopped at the stitch thread line (0.6 to 1.0%). Following that, the delaminations slowly extended toward the center of the specimens. Note that the delamination occurred from one free edge in the stitched specimen (upper side of Fig. 6(a)) because a stitch thread was located near an edge (lower side).

The results demonstrated that the stitching did not affect the onset and accumulation of the ply cracks, but that it did suppress the delamination progress effectively.

3. ANALYSIS

This study adapted the numerical damage-simulation method proposed by Yashiro *et al*. [13] to the stitched laminate. The method is based on finite element analysis using cohesive elements. A cohesive element is the cohesive zone model, which is introduced between the solid elements to eliminate the stress singularity around the crack tip and express the creation of crack surfaces. The cohesive element generates the cohesive traction that resists the increase of the relative displacement between the solid elements. The virtual work principle used in this study is

$$\int_V \mathbf{S} : \delta\mathbf{E}\,\mathrm{d}V + \int_{S_{\mathrm{coh}}} \mathbf{T} \cdot \delta\boldsymbol{\Delta}\,\mathrm{d}S = \int_{S_t} \mathbf{f} \cdot \delta\mathbf{u}\,\mathrm{d}S, \tag{2}$$

where $\mathbf{S}$ and $\mathbf{E}$ are the stress tensor and strain tensor of the solid elements, $\mathbf{T}$ and $\boldsymbol{\Delta}$ are the traction vector and relative displacement vector of the cohesive elements,

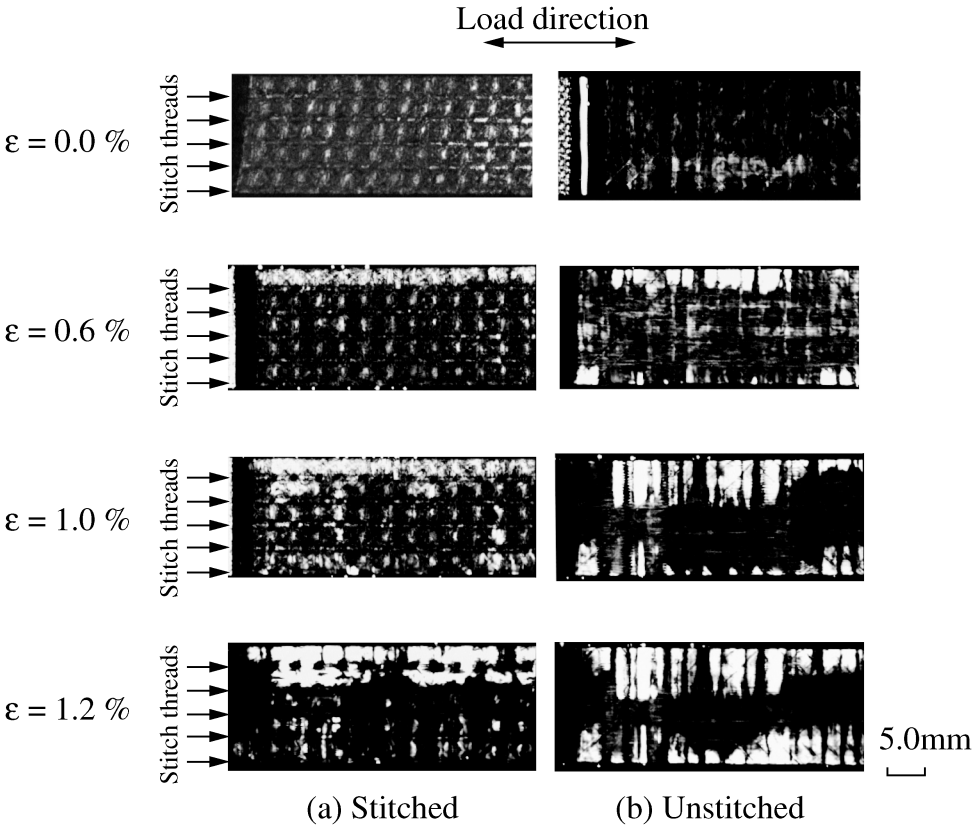

Figure 6. C-scanned images of the specimens. Delamination in the stitched specimen was smaller than that of the unstitched one.

and **f** and **u** are the external force vector and the displacement vector, respectively. S_{coh} means the area where cohesive elements are introduced, and S_t is the area where the external force is applied.

By using the parameter s, the relationship between the traction and relative displacement is expressed as [15]

$$T_i = \frac{s}{1-s}\frac{\Delta_i}{\Delta_{ic}}\sigma_{i\,\max} \quad (i = n, t, b), \tag{3}$$

where index n denotes the normal tensile, t the in-plane shear, and b the out-of-plane shear deformation modes (Fig. 7). Δ_{ic} is the critical relative displacement. When Δ_i becomes equal to Δ_{ic}, the traction completely disappears. $\sigma_{i\,\max}$ is the strength for each deformation mode. The parameter s in equation (3) is calculated as

$$s = \max\bigl(0, \min(s_{\text{ini}}, 1 - D)\bigr), \tag{4}$$

$$D = \sqrt{(\Delta_n/\Delta_{nc})^2 + (\Delta_t/\Delta_{tc})^2 + (\Delta_b/\Delta_{bc})^2}. \tag{5}$$

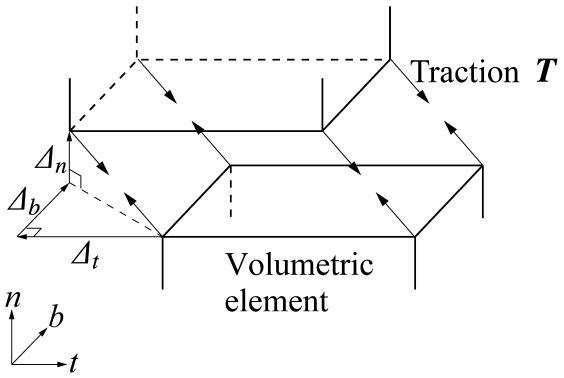

Figure 7. Schematic of a cohesive element.

The parameter s expresses the residual strength of the cohesive element. s_{ini} is the initial value of s, and it is set very close to 1 (in this study, $s_{\text{ini}} = 0.999$). The cohesive element absorbs the energy equal to the critical energy release rate per unit area. Therefore, the critical relative displacements are calculated as

$$\Delta_{nc} = \frac{2G_{\text{Ic}}}{\sigma_{n\,\max} s_{\text{ini}}}, \quad \Delta_{tc} = \frac{2G_{\text{IIc}}}{\sigma_{t\,\max} s_{\text{ini}}}, \quad \Delta_{bc} = \frac{2G_{\text{IIIc}}}{\sigma_{b\,\max} s_{\text{ini}}}, \tag{6}$$

where G_{ic} ($i = \text{I}, \text{II}, \text{III}$) is the critical energy release rate for each deformation mode. The cohesive element behaves as the penalty element when the relative displacement is so small that the parameter s is equal to s_{ini}. When the relative displacement grows larger, parameter s and the traction decrease. When s becomes equal to zero, the cohesive element absorbs the energy equal to the critical energy release rate, and the crack surfaces are created.

By discretizing equation (2), the virtual work principle is expressed in matrix form as

$$(\mathbf{K} + \mathbf{K}_{\text{coh}})\mathbf{U} = \mathbf{F}, \tag{7}$$

where $\mathbf{K}$ and $\mathbf{K}_{\text{coh}}$ denote the stiffness matrices of the solid elements and the cohesive elements, $\mathbf{U}$ is the nodal displacement vector, and $\mathbf{F}$ is the nodal force vector. The stiffness matrix of the cohesive elements $\mathbf{K}_{\text{coh}}$ is calculated as

$$\mathbf{K}_{\text{coh}} = \int_{S_{\text{coh}}} (\mathbf{LN})^T \mathbf{D}_{\text{coh}} (\mathbf{LN})\, \mathrm{d}S, \tag{8}$$

$$\mathbf{D}_{\text{coh}} = \begin{bmatrix} \frac{s}{1-s}\frac{\sigma_{n\,\max}}{\Delta_{nc}} & 0 & 0 \\ 0 & \frac{s}{1-s}\frac{\sigma_{t\,\max}}{\Delta_{tc}} & 0 \\ 0 & 0 & \frac{s}{1-s}\frac{\sigma_{b\,\max}}{\Delta_{bc}} \end{bmatrix}, \tag{9}$$

where $\mathbf{L}$ is the matrix that expresses the relationship between the relative displacement vector $\boldsymbol{\Delta}$ and the displacements of the upper and lower surfaces of the cohesive element, and $\mathbf{N}$ is the matrix created by arranging the shape functions. In

equation (7), the parameter s of each cohesive element changes accompanying the nodal displacement $\mathbf{U}$. Therefore, equation (7) is a nonlinear equation.

Nonlinear equations are usually analyzed by the incremental analysis (further detail is described in the appendix). However, in equation (7), the nonlinearity appears only in ($\mathbf{K}_{\text{coh}}$) because the stitched laminate can be treated as the linear elastic. Therefore, we can obtain the solution of nonlinear equation (7) by using the direct recurrent method [16], which consists of the repetition of linear analyses. Figure 8 illustrates the flowchart of the simulation. First, we set the initial value of parameter s, and apply the boundary conditions. We then make the total stiffness matrix, solve equation (7), and we update the parameter s using the solution. The

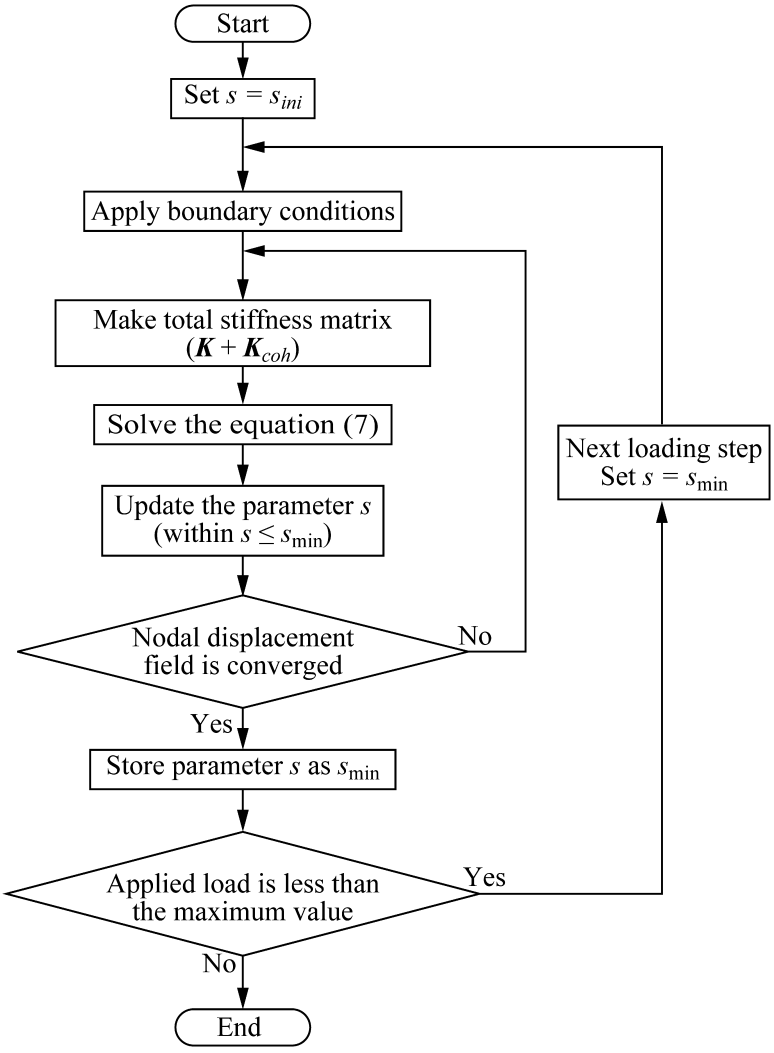

Figure 8. Flowchart of the damage extension simulation.

direct recurrent method solves the equation by repeating these calculations until the displacement converges. We calculate the value of parameter s by using the converged displacement and we use it as the initial value of s in the next loading step. To prevent recovery of the fracture process, we apply a requirement that parameter s cannot have a value greater than the value in the previous loading step ($s \leqslant s_{\min}$) when we update the parameter s.

4. VERIFICATION OF THE NUMERICAL METHOD

In the previous work [13], the numerical method described in the previous section was not verified by fracture mechanics. However, the method differs greatly from the conventional method for solving nonlinear equations because the present method solves the nonlinear equation by repeating the linear equations. Therefore, in this section, we confirm the validity of the method by comparing the two kinds of crack extensions to the theoretical solutions calculated from the linear fracture mechanics following the approach performed by Majima and Suemasu [17].

4.1. Progress of a circular crack in an isotropic infinite solid

Consider the problem illustrated in Fig. 9(a). A circular crack of radius a exists in an isotropic infinite solid, and the uniform pressure σ_0 is applied on part of the crack surface (the circular region of radius b). The theoretical solution [18] demonstrates that the energy release rate becomes smaller when the crack grows larger under a fixed-pressure condition. Thus, in this situation, the crack grows stably in pure mode I.

Figure 9(b) illustrates an example of the finite element models used in the simulations. Considering axisymmetry, the model was divided by the square four-node axisymmetric isoparametric elements. Cohesive elements were introduced at the interface of $z = 0$ mm, $r \leqslant 60$ mm to express the crack. An initial crack of radius 8 mm was assumed, and the pressure was applied at the area of $r \leqslant 4$ mm.

Young's modulus of the isotropic elastic solid was 70 GPa, and Poisson's ratio was 0.3. The mode I strength of the cohesive element $\sigma_{n\max}$ was fixed at 100 MPa, and the mode I critical energy release rate was varied ($G_{\mathrm{Ic}} = 0.2, 1.0, 5.0$ kJ/m^2). Note that pure mode I crack growth was considered in this analysis, and we assigned enough large values to the mode II strength and critical energy release rate. We investigated the effect of the mesh size on the crack extension by analyzing the three models, which had three different sizes of elements (1 mm, 2 mm, and 4 mm).

Figure 10 presents the crack radius as a function of the external force applied on the crack surface. In the numerical results, the crack radius means the radius of the completely fractured cohesive elements (the parameter $s = 0$). Solid lines denote the theoretical solutions. When the critical energy release rate was small, the numerical results did not depend on element size, but they agreed well with the theoretical results. As the critical energy release rate became larger, a larger

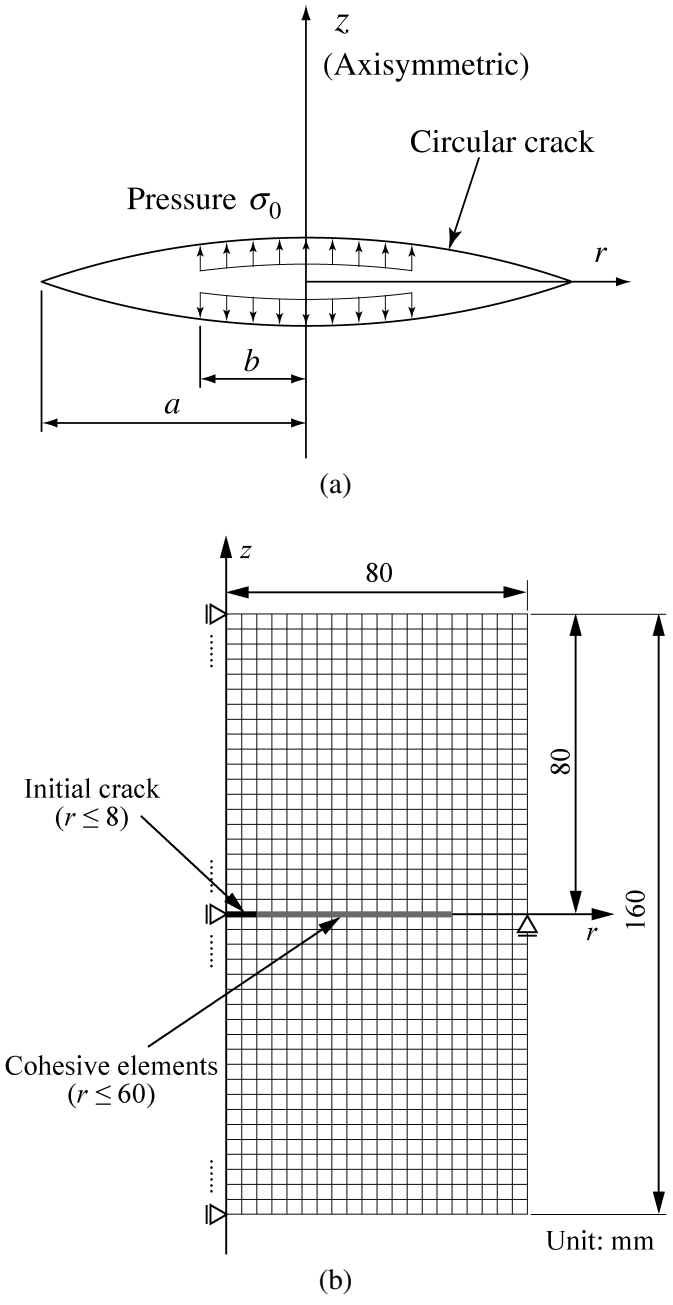

Figure 9. Infinite isotropic material with a circular crack. (a) Schematic of the circular crack. (b) Finite element model.

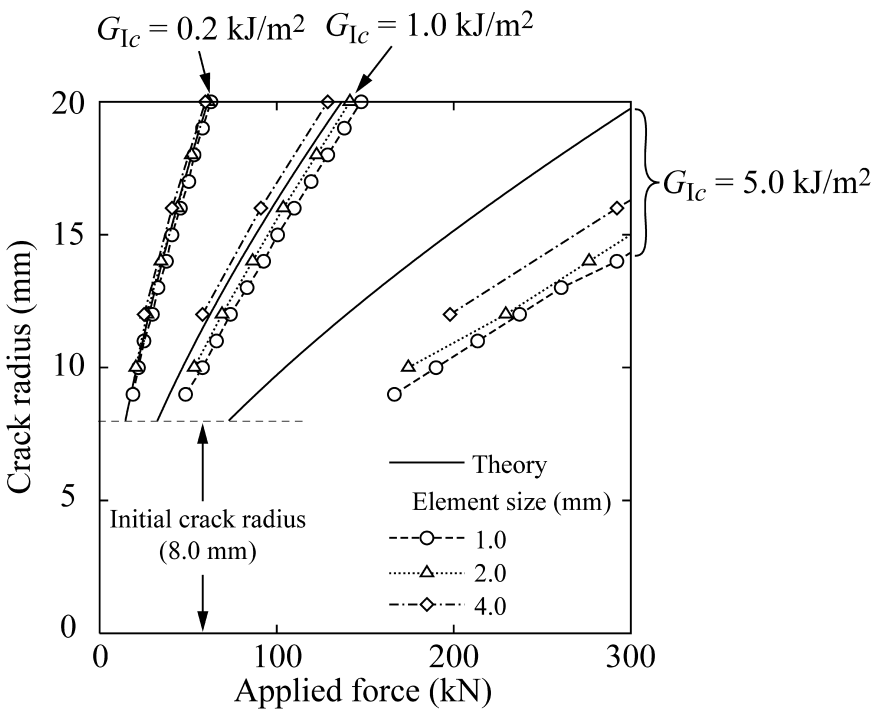

Figure 10. Comparisons of the crack growth among various element sizes and fracture toughness.

load than in the theoretical results was needed to extend the crack to the specific length. Generally, in the small scale yielding fracture, the size of the plastic region at the crack tip is in proportion to the square of the stress intensity factor, namely, the energy release rate [18]. Therefore, if the critical energy release rate is larger, the size of the cohesive zone is larger, and larger inelastic deformation occurs. This is why the difference between the numerical results and solution of the linear fracture mechanics became larger for greater critical energy release rates.

The above results demonstrate that the present numerical method is able to express the equivalent crack extension with linear fracture mechanics when mode I is dominant.

4.2. Progress of a crack in a circular plate loaded from an out-of-plane direction

Consider the crack extension when an out-of-plane load is applied to a boundary-clamped circular plate that has a circular crack at the center (Fig. 11(a)). The theoretical solution [19] demonstrates that the energy release rate of the crack extension is independent of the crack radius. The load needed to extend the crack is decided from the critical energy release rate and the bending stiffness of the plate. In this situation, the crack extends in pure mode II.

Figure 11(b) presents an example of the finite element models used in the present simulations. The model was divided by the square four-node axisymmetric

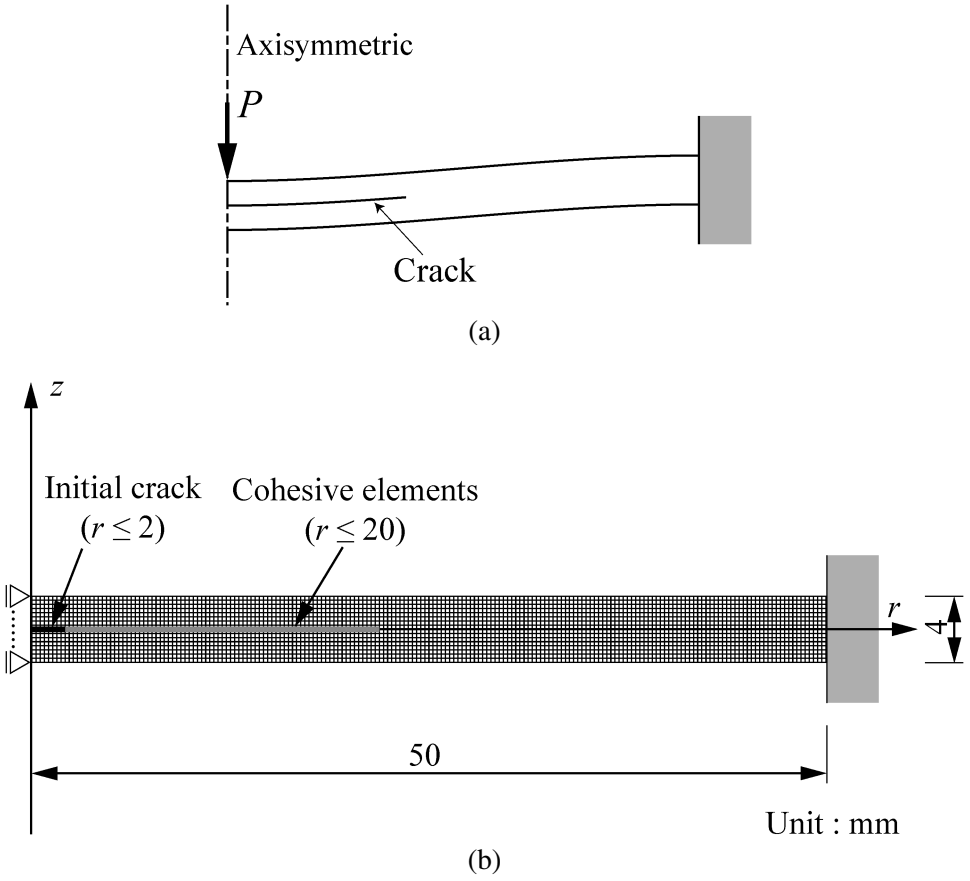

Figure 11. A circular plate with an initial crack subjected to out-of-plane loading. (a) Schematic. (b) Finite element mesh.

isoparametric elements. Cohesive elements were introduced at the interface of $z = 0$ mm and $r \leqslant 20$ mm. An initial crack of radius 2 mm was assumed, and a uniform displacement ($-z$ direction) was applied at the nodes located on the upper surface ($z = 2$ mm) of $r \leqslant 0.5$ mm. The applied load was calculated by summing up the reaction forces of these nodes.

The plate was modeled by in-plane isotropic homogeneous material; the material properties are denoted in Table 1, in which the strengths and critical energy release rates of the cohesive elements are also indicated. We investigated the mesh-size dependency by varying the sizes of the elements (0.25 mm, 0.125 mm, and 0.0625 mm).

Figure 12(a) plots both the simulated and theoretical calculated crack radii as functions of the applied load. In the simulated results, the crack began to extend at a lower load than the theoretical results. As the crack radius became larger, the load that was needed to extend the crack asymptotically approached the theoretical value.

Table 1.
Material properties used in the simulation for the crack growth in the circular plate

In-plane Young's modulus $E_x = E_y$ (GPa)	56.5
Out-of-plane Young's modulus E_z (GPa)	9.15
In-plane Poisson's ratio ν_{xy}	0.316
Out-of-plane Poisson's ratio $\nu_{xz} = \nu_{yz}$	0.262
Out-of-plane shear modulus $G_{xz} = G_{yz}$ (GPa)	4.18
Mode-I cohesive strength $\sigma_{n\,\max}$ (MPa)	32.6
Mode-II cohesive strength $\sigma_{t\,\max}$ (MPa)	85.0
Mode-I critical energy release rate G_{Ic} (J/m^2)	200
Mode-II critical energy release rate G_{IIc} (J/m^2)	400

The load at which the crack began to extend did not have the mesh-size dependency. Figure 12(b) indicates the relationship between the load and deflection, where we used the z-direction displacement of the node located at the center of the lower surface $(r, z) = (0, -2)$ as the deflection. Because the theoretical result is based on the Kirchhoff plate theory, the initial gradient differs from the actual value by about 20% [17]. Considering this, the present analysis provided a valid result regardless of mesh size.

The above results and the results in Section 4.1 demonstrate that the numerical method described in Section 3 can provide the equivalent crack extension with linear fracture mechanics when either mode I or II is dominant.

5. DAMAGE EXTENSION SIMULATION OF THE STITCHED CFRP LAMINATE

Figure 13 depicts the layer-wise finite element model [13] that expressed the stitched laminate. The stacking sequence was $[-45/45/0_3/90_4]_s$. The laminate was divided into four layers, and each layer expressed the ply (plies) of each fiber direction. Each layer was divided by the four-node isoparametric Mindlin plate elements. We assumed that the model was symmetric in the thickness direction (z direction). The stitch threads were expressed by connecting the neighboring layers by two-node Timoshenko beam elements (Fig. 13(b)) and the beam section was circular.

To express the ply cracks in the 90° ply, four-node cohesive elements were introduced every 0.75 mm in the x direction as indicated in Fig. 13(c). In addition, eight-node cohesive elements were introduced at each interface of the layers to connect the layers and to express the delamination. Uniform tensile displacement was applied on the end surface of the finite element model in the x direction. We performed numerical analysis using the method described in Section 3. The damage progress of the model with stitch threads (beam elements) was compared to that of the model without threads.

The material properties and the properties of the cohesive elements used in this analysis are presented in Tables 2 and 3. The values of the critical energy release rates in Table 3 were decided by fitting the damage progress to the experimental

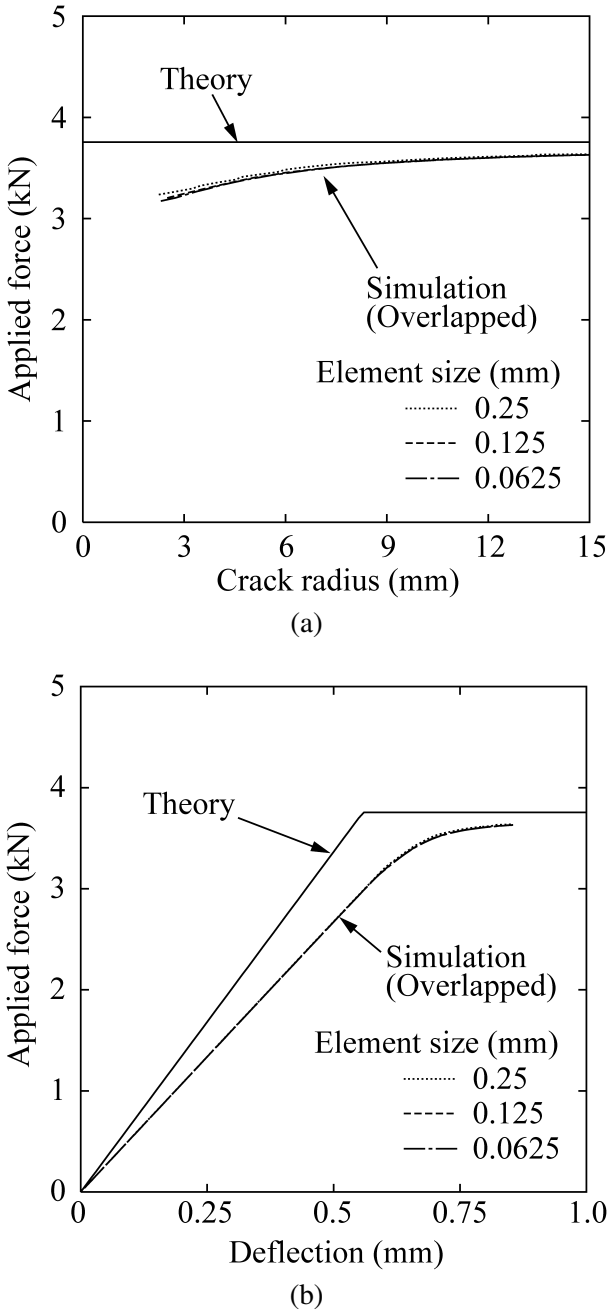

Figure 12. Simulated results of the crack growth in a circular plate. (a) Crack propagation. (b) Load - deflection relation.

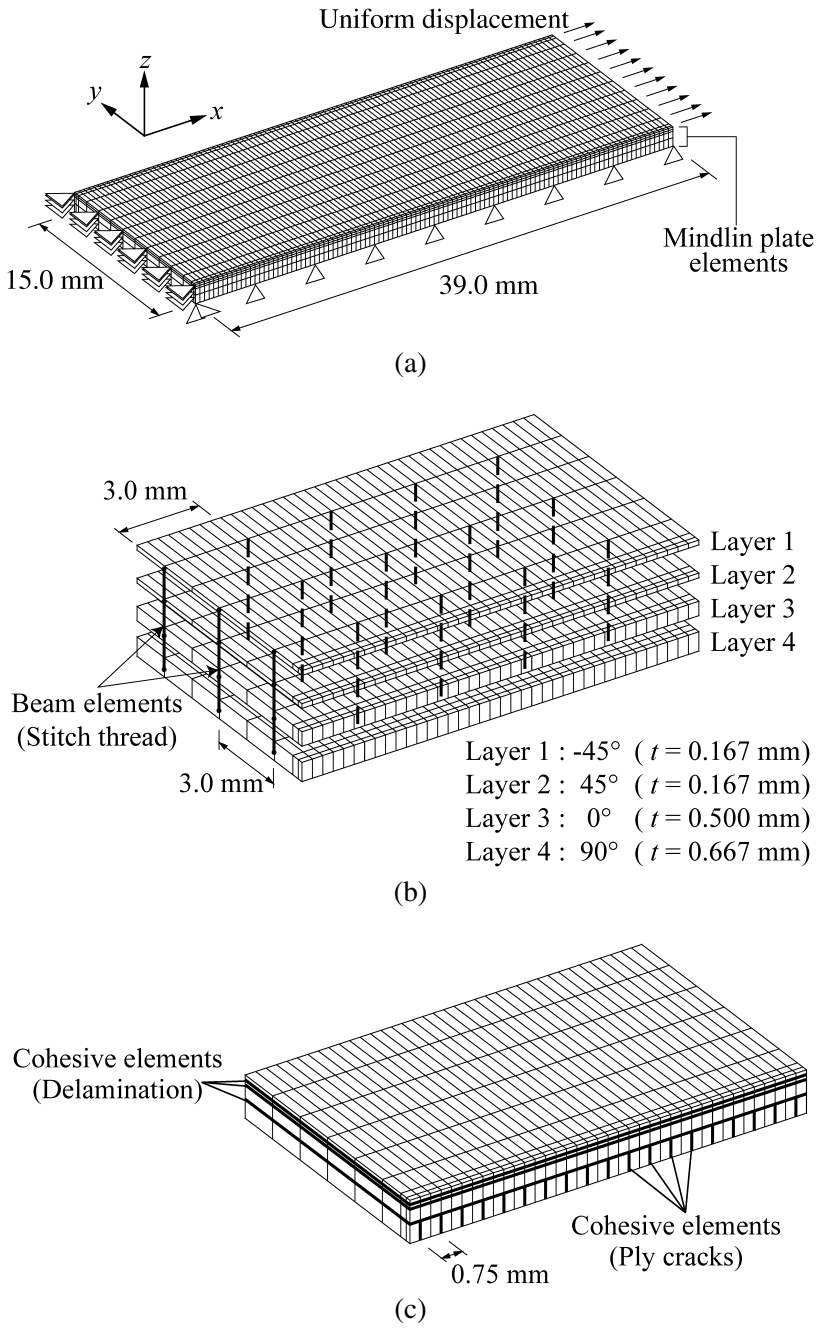

Figure 13. Layer-wise finite element model of a stitched laminate with cohesive elements. (a) Overview of the mesh. (b) Beam elements (magnified view). (c) Cohesive elements (magnified view).

Table 2.
Material properties of a stitched laminate

Laminate	
Longitudinal Young's modulus (GPa)	144.65
Transverse Young's modulus (GPa)	9.57
In-plane shear modulus (GPa)	4.50
Out-of-plane shear modulus (GPa)	3.50
In-plane Poisson's ratio	0.356
Out-of-plane Poisson's ratio	0.49
Stitch thread	
Young's modulus (GPa)	148.0
In-plane shear modulus (GPa)	4.5
Diameter (mm)	1.5

Table 3.
Properties of the cohesive elements used in the damage extension simulation

	Ply crack	Delamination
In-plane tensile strength (Mode I, MPa)	15.0	30.0
In-plane shear strength (Mode II, MPa)	40.0	60.0
Out-of-plane shear strength (Mode III, MPa)	40.0	60.0
Critical energy release rate (Mode I, J/m^2)	100.0	150.0
Critical energy release rate (Mode II, III, J/m^2)	500.0	750.0

results of the stitched specimen. Figure 5 plots the crack densities as functions of the applied strain. The ply cracks, which were longer than 70% of the model width, were considered to be penetrated cracks. The crack densities began to increase sharply at 0.5% strain, and after 0.8% strain, continued to increase slowly. No difference of crack densities was observed between the stitched and unstitched models. These numerical results agreed well with the experimental results, confirming the experimental results that onset and accumulation of the ply cracks were not affected by the stitching. In Fig. 5, we considered the cracks that were longer than 70% of the model width to be penetrated, and verified that results did not change even if we changed the threshold for penetration.

Figure 14 displays the numerical results for the delamination at the 0°/90° interface. The points in the figure denote the cohesive elements, which fractured completely (the residual strength parameter $s = 0$). In both stitched and unstitched models, delamination occurred at the edge of the model in the width direction at the tip of the ply crack in the 90° layer at 0.65% strain. In the stitched model, the delamination progress stopped at the stitch thread line. As strain increased, the delamination gradually extended toward the center of the specimen. The delamination avoided the stitch threads. In the unstitched model, the delamination quickly extended toward the center of the model almost simultaneously with the onset of the delamination. The damage progress agreed well with the experimental

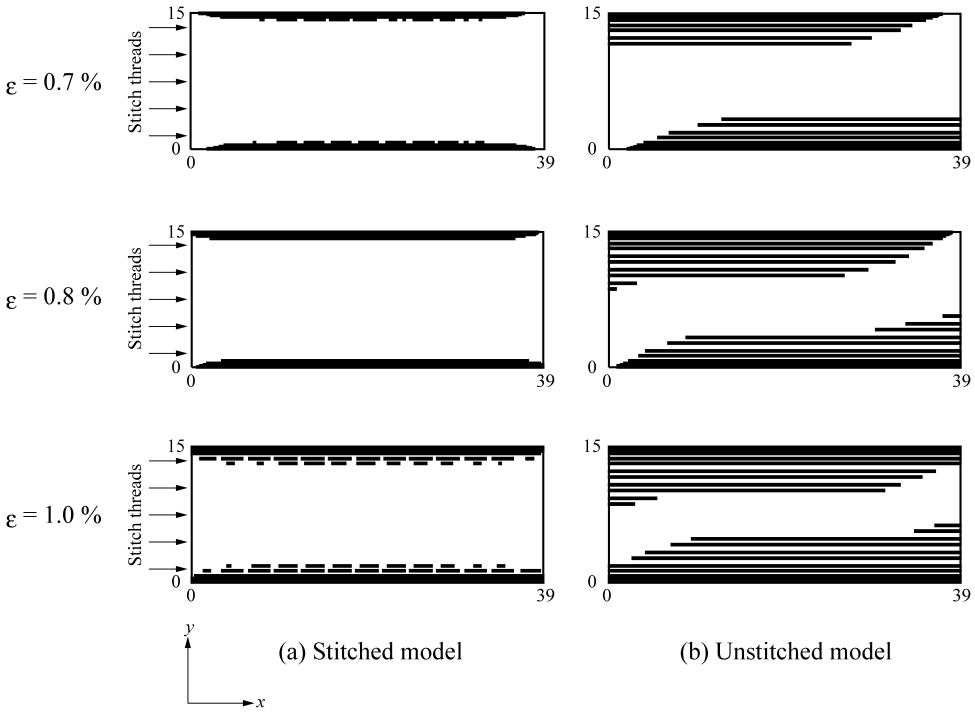

Figure 14. Simulated delamination propagation at the 0°/90° ply interface.

results (Figs 4 and 6). However, the delamination shape of the unstitched model differed from the experimental results, extending on a slant away from the length direction of the specimen. In the experiment, the specimen was gripped at the GFRP tab (left side of the photographs in Fig. 6). The specimen was thus constrained in the thickness direction at this region. This difference in constraint in the thickness direction was the reason for the difference of the delamination shapes between experiment and the simulation.

In the unstitched model, even small load increments extended the delamination largely because the displacement of the ±45° layers in the out-of-plane direction opened the delamination that occurred at the tip of the ply crack. However, in the stitched model, stitch threads suppressed the displacement of the ±45° layers in the out-of-plane direction. The delamination was mainly extended by the shear deformation between the layers at the tip of the ply crack. In addition, this shear deformation was suppressed near the stitch thread. Therefore, delamination did not extend beyond the stitch threads.

6. CONCLUSION

The present paper experimentally and numerically investigated the tensile damage progress in stitched laminates.

(1) Regardless of stitching, ply cracks and delamination were observed in the laminate composites under tensile load. Onset and accumulation of the ply cracks were not affected by the stitching. The delamination area of the stitched laminate was smaller than that of the unstitched one.

(2) We demonstrated that finite element analysis with cohesive elements could provide the equivalent crack extension to the linear fracture mechanics by using a method that consists of the repetition of linear analysis.

(3) Onset and progress of the ply cracks and the delamination obtained from the damage extension simulation to the stitched laminates agreed well with the experimental results. In particular, we verified that the stitch threads suppressed the extension of delamination.

Acknowledgement

A. Yoshimura is supported by the Ministry of Education, Culture, Sports, Science and Technology of Japan under a Grant-in-Aid for Scientific Research (No. 16-11471).

REFERENCES

1. L. Jain and Y. W. Mai, On the effect of stitching on mode I delamination toughness of laminated composites, *Compos. Sci. Technol.* **51**, 331–345 (1994).
2. L. Jain and Y. W. Mai, Determination of mode II delamination toughness of stitched laminated composites, *Compos. Sci. Technol.* **55**, 241–253 (1995).
3. K. A. Dransfield, L. K. Jain and Y. W. Mai, On the effects of stitching in CFRPs – I. Mode I delamination toughness, *Compos. Sci. Technol.* **58**, 815–827 (1998).
4. Y. Iwahori, T. Ishikawa, Y. Hayashi and N. Watanabe, Study of interlaminar fracture toughness improvement on stitched CFRP laminates, *J. Japan Soc. Compos. Mater.* **26**, 90–100 (2000).
5. L. Chen, P. G. Ifju and B. V. Sankar, Analysis of mode I and mode II tests for composites with translaminar reinforcements, *J. Compos. Mater.* **39**, 1311–1333 (2005).
6. E. Wu and J. Wang, Behavior of stitched laminates under in-plane tensile and transverse impact loading, *J. Compos. Mater.* **29**, 2254–2279 (1995).
7. F. Aymerich, P. Priolo and C. T. Sun, Static and fatigue behaviour of stitched graphite/epoxy composite laminates, *Compos. Sci. Technol.* **63**, 907–917 (2003).
8. M. Z. Shah Khan and A. P. Mouritz, Fatigue behaviour of stitched GRP laminates, *Compos. Sci. Technol.* **56**, 695–701 (1996).
9. F. Larsson, Damage tolerance of a stitched carbon/epoxy laminate, *Composites Part A* **28A**, 923–934 (1997).
10. N. A. Warrior, C. D. Rudd and S. P. Gardner, Experimental studies of embroidery for the local reinforcement of composites structures 1. Stress concentrations, *Compos. Sci. Technol.* **59**, 2125–2137 (1999).
11. N. Takeda and S. Ogihara, *In situ* observation and probabilistic prediction of microscopic failure processes in CFRP cross-ply laminates, *Compos. Sci. Technol.* **52**, 183–195 (1994).
12. T. Okabe, H. Sekine, J. Noda, M. Nishikawa and N. Takeda, Characterization of tensile damage and strength in GFRP cross-ply laminates, *Mater. Sci. Engng A – Struct* **383**, 381–389 (2004).

13. S. Yashiro, N. Takeda, T. Okabe and H. Sekine, A new approach to predicting multiple damage states in composite laminates with embedded FBG sensors, *Compos. Sci. Technol.* **65**, 659–667 (2005).
14. R. Kamiya, B. A. Cheeseman, P. Popper and C. T. Wei, Some recent advantages in the fabrication and design of three-dimensional textile preforms: a review, *Compos. Sci. Technol.* **60**, 33–47 (2000).
15. P. H. Geubelle and J. S. Baylor, Impact-induced delamination of composites: a 2D simulation, *Composites Part B* **29**, 589–602 (1998).
16. D. R. J. Owen, *Finite Elements in Plasticity*. Pineridge Press, Swansea (1980).
17. O. Majima and H. Suemasu, A finite element analysis of delamination propagation in composite laminates, *J. Japan Soc. Compos. Mater.* **25**, 140–148 (1999).
18. H. Okamura, *An Introduction to Linear Fracture Mechanics*. Baifukan, Tokyo (1976).
19. H. Suemasu and O. Majima, Multiple delaminations and their severity in circular axisymmetric plates subjected to transverse loading, *J. Compos. Mater.* **30**, 441–453 (1996).
20. Y. Yamada, N. Yoshimura and T. Sakurai, Plastic stress–strain matrix and its application for the solution of elastic–plastic problems by the finite element method, *Int. Mech. Sci.* **10**, 343–354 (1968).
21. M. A. Crisfield, G. Jelenic, Y. Mi, H. G. Zhong and Z. Fan, Some aspects of the nonlinear finite element method, *Finite Elem. Anal. Des.* **27**, 19–40 (1997).

APPENDIX

By taking the time differential $(\cdot)$ of the equivalent nodal force vector $\mathbf{Q}$ $(=\mathbf{F})$, and considering the increment during the infinitesimal time $\mathrm{d}t$, we obtain the linearized equation between the time t and $t+\mathrm{d}t$ as

$$\dot{\mathbf{Q}}\,\mathrm{d}t = \left(\frac{\partial \mathbf{Q}}{\partial \mathbf{U}}\right)\dot{\mathbf{U}}\,\mathrm{d}t = \dot{\mathbf{F}}\,\mathrm{d}t, \tag{10}$$

$$(\tilde{\mathbf{K}} + \tilde{\mathbf{K}}_{\mathrm{coh}})\underline{\mathbf{U}} = \underline{\mathbf{F}}, \tag{11}$$

where $\tilde{\mathbf{K}}$ denotes the tangential stiffness matrix of the solid elements, and underline means the increment. The tangential stiffness matrix of the cohesive elements $\tilde{\mathbf{K}}_{\mathrm{coh}}$ is calculated as

$$\tilde{\mathbf{K}}_{\mathrm{coh}} = \int_{S_{\mathrm{coh}}} (\mathbf{LN})^T \frac{\partial \mathbf{T}}{\partial \boldsymbol{\Delta}} (\mathbf{LN})\,\mathrm{d}S. \tag{12}$$

The matrix $\partial\mathbf{T}/\partial\boldsymbol{\Delta}$ is written as

$$\frac{\partial \mathbf{T}}{\partial \boldsymbol{\Delta}} = \begin{bmatrix} \frac{s}{1-s}\frac{\sigma_{n\max}}{\Delta_{nc}} & 0 & 0 \\ 0 & \frac{s}{1-s}\frac{\sigma_{t\max}}{\Delta_{tc}} & 0 \\ 0 & 0 & \frac{s}{1-s}\frac{\sigma_{b\max}}{\Delta_{bc}} \end{bmatrix} \quad (s = s_{\mathrm{ini}} = const.), \tag{13a}$$

$$\frac{\partial \mathbf{T}}{\partial \boldsymbol{\Delta}} = \begin{bmatrix} \left(\frac{s}{1-s} - \frac{\Delta_n^2/\Delta_{nc}^2}{(1-s)^3}\right)\frac{\sigma_{n\max}}{\Delta_{nc}} & -\frac{\Delta_n\Delta_t/\Delta_{tc}^2}{(1-s)^3}\frac{\sigma_{n\max}}{\Delta_{nc}} & -\frac{\Delta_n\Delta_b/\Delta_{bc}^2}{(1-s)^3}\frac{\sigma_{n\max}}{\Delta_{nc}} \\ -\frac{\Delta_t\Delta_n/\Delta_{nc}^2}{(1-s)^3}\frac{\sigma_{t\max}}{\Delta_{tc}} & \left(\frac{s}{1-s} - \frac{\Delta_t^2/\Delta_{tc}^2}{(1-s)^3}\right)\frac{\sigma_{t\max}}{\Delta_{tc}} & -\frac{\Delta_t\Delta_b/\Delta_{bc}^2}{(1-s)^3}\frac{\sigma_{t\max}}{\Delta_{tc}} \\ -\frac{\Delta_b\Delta_n/\Delta_{nc}^2}{(1-s)^3}\frac{\sigma_{b\max}}{\Delta_{bc}} & -\frac{\Delta_b\Delta_t/\Delta_{tc}^2}{(1-s)^3}\frac{\sigma_{b\max}}{\Delta_{bc}} & \left(\frac{s}{1-s} - \frac{\Delta_b^2/\Delta_{bc}^2}{(1-s)^3}\right)\frac{\sigma_{b\max}}{\Delta_{bc}} \end{bmatrix} \quad (s \neq const.). \tag{13b}$$

Therefore, in the incremental analysis, we have to search for the time increment causes the transition of the condition in equation (13). For this search, a special method (such as the $R_{\min}$ method [20]) is needed. In addition, for stable analysis, special consideration of the transition of the condition in the convergence calculation is required. Moreover, Crisfield *et al.* [21] pointed out that numerical instability occurs because equation (13b) contains softening behavior (negative stiffness).